Received 20 June 2025; revised 18 July 2025; accepted 28 July 2025. Date of publication 1 August 2025; date of current version 24 November 2025.

Digital Object Identifier 10.1109/OJAP.2025.3594893

Design of a Wideband Transmitarray (TA) Antenna With Subwavelength Thin Metasurface

SOUGATA CHATTERJEE [1] (Graduate Student Member, IEEE), YASHWANT GUPTA [2] (Senior Member, IEEE), SATISH K. SHARMA [3] (Fellow, IEEE), AND SOMAK BHATTACHARYYA [1] (Senior Member, IEEE)

[1]Department of Electronics Engineering, Indian Institute of Technology-BHU, Varanasi 221005, India
[2]National Center for Radio Astrophysics-TIFR, Pune 411007, India
[3]Department of Electrical and Computer Engineering, San Diego State University, San Diego, CA 92182, USA

CORRESPONDING AUTHORS: S. BHATTACHARYYA AND S.K. SHARMA (e-mail: somakbhattacharyya.ece@iitbhu.ac.in; ssharma@sdsu.edu)

ABSTRACT This report presents the design of a high-performance wideband transmitarray (TA) antenna featuring a low-profile, 2-bit subwavelength metasurface (MS) array. The antenna employs an optimized Potter horn (PH) as the source feed and an innovative metasurface structure, enabling seamless 360° phase coverage with 90° linear phase variations. The metasurface is constructed using three metallic layers on RT/Duroid 5880 substrates, with polarization-selective top and bottom surfaces and a polarization-rotating middle layer incorporating a 45° rotated dipole resonator and a square ring corner cut. A wideband response is achieved using the generalized scattering matrix (GSM) method, while the mixed-integer sequential optimization ensures optimal tapering of the PH feed. The circular aperture design, comprising 729 elements, is guided by the generalized phase distribution method. The antenna exhibits exceptional performance with a peak gain of 27.2 dBi, aperture efficiency (AE) of 58.5% at 32 GHz, and sidelobe levels suppressed below –24 dB across the operational band. Notably, the 1-dB and 3-dB gain bandwidth (GBWs) are 12.69 GHz (39.68%) and 15.84 GHz (49.2%), respectively. Fabrication and experimental validation confirm reasonably good agreement with simulation results, emphasizing the TA antenna's robustness and reliability. Its advanced design and superior performance make it ideal for applications in Ka-band radio astronomy and space communication.

INDEX TERMS Aperture efficiency (AE), cross polar (CP) transmission, metasurface (MS), transmitarray (TA) antenna.

I. INTRODUCTION

TRANSMITARRAY (TA) antennas, owing to their high profile, portability, and high-gain characteristics, have emerged as versatile solutions for diverse applications such as wireless communication [1], radar [2], and target tracking [3] to deliver precise beam control and high directivity. The performance of a TA antenna is quantified by its figure of merit (FoM), encompassing metrics such as overall gain, aperture efficiency (AE), gain bandwidths (GBWs) for 1-dB and 3-dB criterion, and sidelobe level (SLL) suppression.

To maximize these performance parameters, researchers have explored various phasing techniques, including frequency-selective surfaces (FSSs) [4], [5], Fabry-Perot (FP) cavity-based FSSs [6], [7], and magneto-electric (ME) dipole configurations, where metallic layers operate as receiver and transmitter components [8], [10]. Additionally, unconventional polarizer conversion elements [11], [12] and polarization rotation (PR) elements [13] are being introduced to further enhance the TA antenna designs.

Most researchers are focusing on designing and modifying the TA unit cell, while comparatively overlooking the feed system—an equally critical component for enhancing the FoM of the TA antenna. As a result, they are achieving high gain, but often at the cost of reduced AE, limited GBWs, and elevated low SLLs.

MS, composed of sub-wavelength periodic structures, enable precise wave manipulation by tailoring the dimensions of their meta-atoms (MAs) [14]. Their compact design makes them ideal for the advanced applications such as antennas, polarization converters, and filters, with significant potential for advanced areas of communications [15], [16], [17], [18].

To achieve wider 1-dB and 3-dB GBWs, with maximized AE and, low SLLs, this paper proposes a wideband, subwavelength low-profile MS array with phase-controlled transmission, fed by a Potter horn (PH) whose edge taper (10 dB) and half power beamwidth (3-dB beamwidth) slowly varying so that provide consistent and uniform illumination across the target frequency range. The MS unit cell integrates a 45°-rotated dipole, a corner-cut square ring, and orthogonal metallic strips, forming a Fabry-Perot resonator (FPR) configuration. While continuous phase modulation can offer higher efficiency, a 2-bit quantized approach was chosen in this work to balance performance with practical fabrication constraints. This composite element undergoes optimization using the Generalized Scattering Matrix (GSM) method [19], which analyzes each layer independently through a cascading approach, offering a broad 2-dB bandwidth and a linear phase response over the desired frequency range enabling enhanced AE and wide GBWs. Concurrently, the PH is refined using a sequential algorithm [20] to ensure a smoothly varying edge taper, enabling low SLLs and further enhanced AE, while maintaining wide 1-dB and 3-dB GBWs. The designed TA antenna exhibits a peak gain of 27.2 dBi, with an AE of 58.5% at 32 GHz and a structure thickness of just 0.157λo at 30 GHz. Notably, the antenna delivers 1-dB and 3-dB GBWs of 39.68% and 49.2%, respectively; thereby offering 15% improvement in AE and 20% enhancement in GBWs compared to the state-of-the-art designs [4], [5], [6], [7], [8], [9], [10], [11], [12]. Fabrication and experimental validation confirm reasonably good agreement with simulations and emphasize the practicality and reliability of the proposed design.

II. FOM IMPROVEMENT OF TA ANTENNA VIA DESIGN OPTIMIZATION

The proposed TA antenna is relying on an optimized feed and accurate aperture phase control TA aperture. Fig. 1 illustrates the ongoing design: (a) functional diagram of the TA antenna, (b) FPR-based MAs, and (c) optimized PH feed.

The FoM of the TA antenna is not improving due to the following reasons: (a) the amplitude decreases while the phase response does not maintain a linear variation across a broad frequency range, resulting narrow GBWs, and (b) the feeder edge taper increases with frequency, resulting in lower SLLs at the expense of reduced AE.

To overcome these limitations and enhance the FoM, the present work is being carried out as follows:

(i) A four-state FPR-MAs element (wider) is being designed to achieve a full 360° phase coverage. The MAs is further optimized using the GSM method, which is effectively enabling a wide 2-dB bandwidth with near-linear

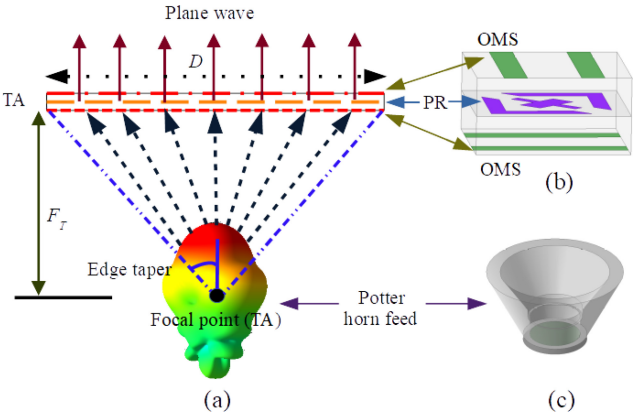

FIGURE 1. (a) Functional diagram of the transmitarray (TA) illustrating key elements for FoM enhancement, (b) FPR based MAs, and (c) optimized potter horn (PH). [OMS stands for orthogonal metallic strip and PR is polarization rotator].

phase variation across a broad frequency range [19]. In this optimization, the lattice dimension is being constrained within 0.3λ–0.4λ to achieve a balanced FoM [21]. While previous works have utilized genetic algorithm (GA)-based optimization [22] and unoptimized approaches [23], they are not demonstrating comparable bandwidth performance and are often more time-consuming than the GSM-based approach. (ii) An optimized PH feed [20] is being designed with a 10 dB edge taper and a slowly varying 3 dB beamwidth over the operating frequency range. Simulation results indicate that a 10 dB edge taper achieves over 60% AE while maintaining low SLLs key parameters for this design choice [21].

The novelty of the proposed TA antenna lies in its systematic co-design methodology. First, an FPR-based MA is being developed and optimized to operate efficiently across the 22–38 GHz band. Next, the TA aperture diameter and focal ratio (F_T/D) are being fixed to ensure optimal focusing. Finally, the PH feed is being carefully optimized to provide consistent and uniform illumination across the entire frequency range. This integrated design approach is resulting in a wide 1-dB and 3-dB GBW, high gain, improved AE, and suppressed SLLs across the operational band.

III. DESIGN OF META ATOM (MA) USING GSM METHOD

The generalized transmission matrix for a linearly polarized incident wave is given in (1), where E_t^x, and E_t^y are the transmitted electric fields for the x- and y- polarized waves, whereas E_i^x and E_i^y are the incident x- and y-polarized electric fields, respectively. $\overline{\overline{T}}$ is a 2×2 transmission matrix defined in (2), where t_{xx} and t_{yy} are co-polarized transmission amplitudes, whereas t_{yx} and t_{xy} are the cross-polarized transmission amplitudes with x or y polarizations.

$$\begin{pmatrix} E_t^x \\ E_t^y \end{pmatrix} = \overline{\overline{T}} \begin{pmatrix} E_i^x \\ E_i^y \end{pmatrix} \tag{1}$$

$$\overline{\overline{T}} = \begin{bmatrix} t_{xx} & t_{xy} \\ t_{yx} & t_{yy} \end{bmatrix} \tag{2}$$

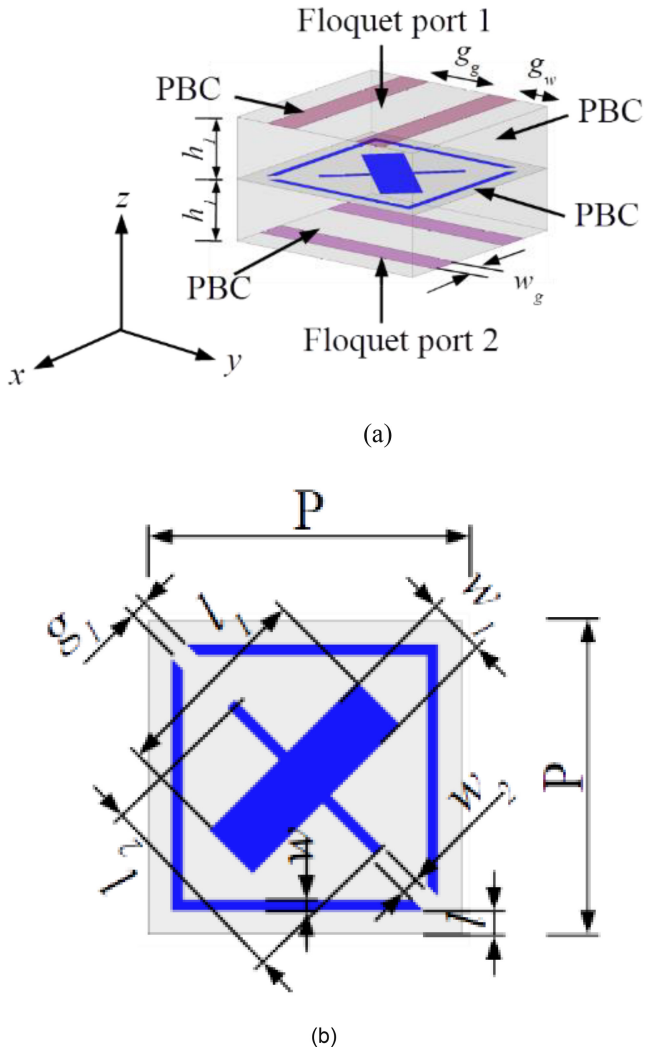

FIGURE 2. (a) 3-D perspective view of the MA and (b) the middle layer of the proposed MA. [For MA_{00}: $P = 3$, $w_1 = 0.58$, $w_2 = 0.1$, $l_1 = 2.0$, $l_2 = 2.0$, $g_1 = 0.2$, $l = 0.22$, $w = 0.1$, MA_{01}: $w_1 = 0.50$, $w_2 = 0.2$, $l_1 = 1.0$, $l_2 = 1.6$, $g_1 = 0.6$, $l = 0.32$, $w = 0.3$; all dimensions are in mm].

Fig. 2(a) illustrates the 3D perspective view of the proposed MA, featuring a three-layered metallic structure sandwiched between two identical RT/Duroid-5880 dielectric substrates ($\varepsilon_r = 2.2$, $\tan\delta = 0.0009$) of thickness $h_1 = 0.787$ mm. The top and bottom metallic layers, with orthogonal patterns, serve as polarization-selective surfaces, enabling transmissive behavior for *y*-polarized waves and reflective behavior for *x*-polarized waves. Each layer shares identical dimensions: width w_g=0.525 mm, gap g_g=1.05 mm, and gap width g_w=0.525 mm.

The middle layer, depicted in Fig. 2(b), incorporates a 45°-rotated dipole resonator with a corner-cut square ring, functioning as a PR. This configuration ensures the *y*-polarized incident wave passes through the top layer, while the middle layer reflects the parallel component and transmits the perpendicular component unaltered through the bottom layer, resulting in the generation of the transmission coefficient t_{xy}. The incident wave undergoes multiple transmissions and reflections between the top and bottom surfaces to interfere destructively on the reflective side, along with a near-unity transmission. The simulation has been carried out in Ansys HFSS 2023 R2 [24], where the PEC material has been considered as the metal layer. The computation process becomes slow for conventional full-wave simulation due to the involvement of many unknown variables in each of the layers [19]. This necessitates the use of the GSM method, in which the responses of properly mode-matched layers are cascaded. Each mode-matching layer is modeled using full-wave simulations to achieve a wideband and flat overall response. To ensure independent control along with broad frequency coverage, the design of the elements should strive to meet several key criteria. First, it is essential to minimize the mutual coupling between elements. In addition, TA elements should exhibit linear phase responses that remain consistent throughout the operational frequency range.

Furthermore, for TA elements, maintaining a transmission magnitude closer to unity ensures minimal signal loss and optimal efficiency. The optimized dimensions of different MAs following the GSM technique are listed in the caption of Fig. 1. By mirroring the middle layer structure along the diagonal axis of the MA as shown in Fig. 2(b), an additional 180° phase shift is introduced. This modification creates two additional MA_{10}, and MA_{11}, achieving a full 360° transmission phase coverage, which is essential for the complete and effective design of the TA aperture. Subwavelength metasurface unit cells enhance AE by enabling precise wavefront control, grating lobe suppression, and low-loss transmission.

Their compact, planar design also supports polarization flexibility and efficient integration for high-performance antenna applications [21]. Fig. 3(a) presents the simulated magnitude and phase responses of the cross-polar amplitude transmission coefficient (t_{xy}) for all the MAs. The magnitude of t_{xy} consistently exceeds 80% (–2 dB) across the frequency range of 22 GHz to 40 GHz. Fig. 3(b) illustrates the co-polar amplitude reflection coefficients (r_{xx} and r_{yy}), showing their corresponding magnitude and phase responses for the MAs. Amplitude overlaps have been observed between MA_{00}, MA_{10} and MA_{01}, MA_{11} pairs, indicating limited distinguishability. The mutual phase difference among the MAs is maintained close to 90° (with a maximum phase imbalance of ±3°), as shown in Fig. 3(a). The MAs exhibit phase discontinuities of ±9° at 31 GHz and ±11.5° at 38.5 GHz. The FPRs exhibit polarization sensitivity, and from Fig. 3(b), the *x*-polarized wave is undergoing nearly complete reflection, with its phase varying consistently across the frequency range. In contrast, the *y*-polarized wave is transmitting through the MAs, generating cross-polarized transmission via the PR elements through constructive interference. The structure is further analyzed under *y*-polarized incidence at various oblique angles (up to 45°). Fig. 4 presents the simulated magnitude (Fig. 4(a) and (c))

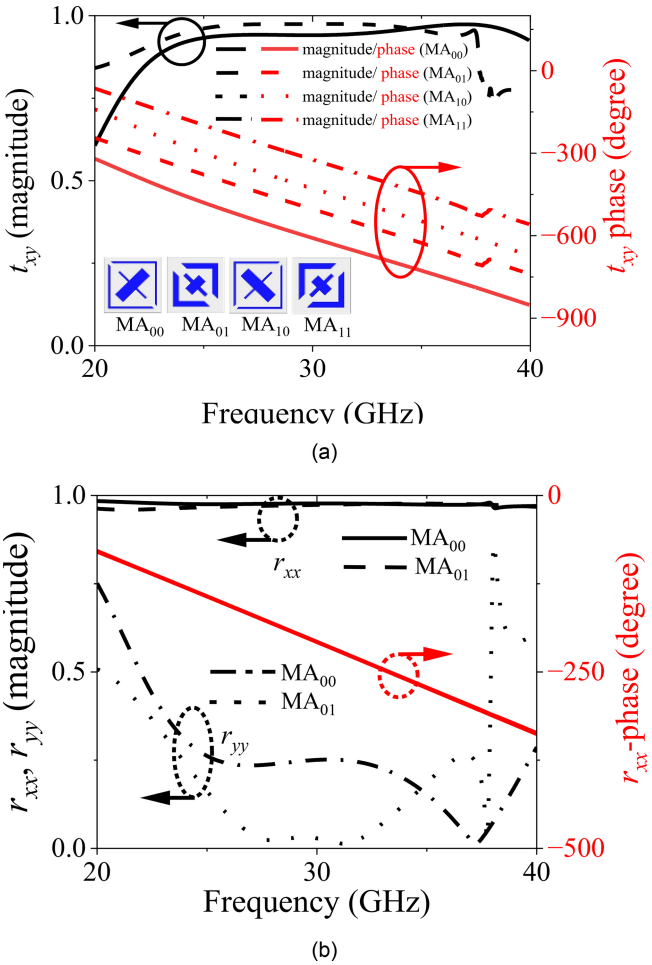

FIGURE 3. (a) Cross-polarized transmission (t_{xy}) magnitude and phase responses and (b) Co-polar reflection (r_{xx}, r_{yy}) magnitude and phase response for the for MA.

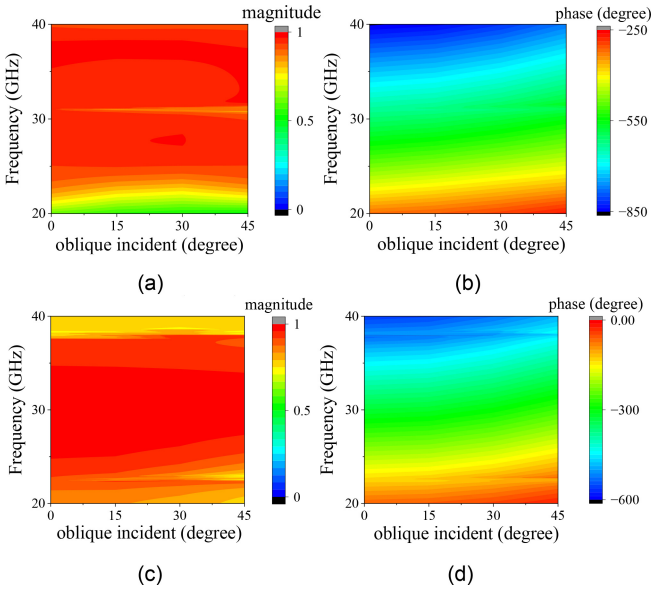

FIGURE 4. Cross-polarized (t_{xy}) responses of (a) magnitude and (b) phase for MA_{00}, and (c) magnitude and (d) phase for MA_{01} under varying oblique incidence angles.

TABLE 1. Electrical size of unit-cell compared to literature study.

Reference	[6]	[7]	[9]	[10]	[12]	[13]	This work
Electrical size	0.5λ	0.46λ	0.38λ	0.44λ	0.44λ	0.44λ	0.33λ

and phase (Fig. 4(b) and 4(d)) responses for all MAs under these conditions.

The results demonstrate a wideband t_{xy} accompanied by a linear phase distribution. However, minor phase discontinuities (31 GHz and 38.5 GHz) were observed with the increase of the incident angle. Fig. 5 illustrates the surface current distributions for MA_{00} and MA_{10} at 31 GHz, and MA_{01} and MA_{11} at 38.5 GHz, under normal and 40° incidence. This analysis is being carried out to investigate the phase discontinuities introduced by the MAs under varying illumination conditions. It can be observed from Fig. 5 that surface currents are minimum at normal incidence, while the presence of the strong currents at 40° incident angle lead to the phase discontinuities. The corner-cut square ring generates strong edge capacitance-induced currents at its gap, with its resonance properties determined by the ring's width and gap dimensions. Increasing the oblique incidence angle enhances current concentration at the gap, reinforcing the resonance (Fig. 5.). Despite this, the phase discontinuities remain minimal, and the amplitude exceeds 80%, ensuring no adverse impact on the overall TA antenna performance. Moreover, to mitigate this, the proposed TA antenna uses a focal ratio (F_T/D) of unity, together with a 10 dB edge taper of 26.5°; thus, ensuring negligible phase discontinuities.

IV. WIDEBAND HIGH GAIN TA ANTENNA DESIGN

A. HORN (PH) DESIGN FOR SOURCE FEED

The source feed in a TA antenna requires moderate gain and wide-beamwidth and wide bandwidth to ensure consistent illumination, accurate phase compensation, and optimal performance across broadband as well as multi-frequency applications. While corrugated horns (CH) are common for wideband applications due to excellent E and H plane matching and low cross-polarization [25], multimode horns offer higher aperture efficiency. Still, they are limited by their complexity and large size [26], [27]. For this design, a Potter horn (PH) was chosen as the source feed, as it supports two modes viz., TE_{11} and TM_{11} at the throat, providing polarization-independent beamwidth and low side-lobe levels (SLL) [28], [29]. The mixed-integer sequential algorithm [20] in HFSS optimizes discrete variables (e.g., mode numbers, corrugations) and continuous dimensions (e.g., radii R_0, R_1, lengths L_1, L_2) to maximize gain and minimize edge taper, enhancing the Potter horn's bandwidth and performance.

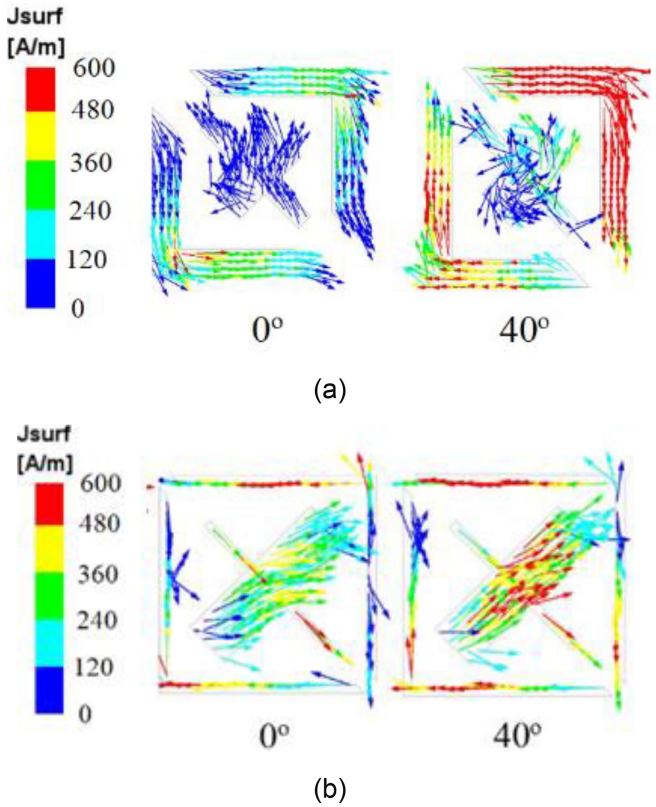

FIGURE 5. Surface current distribution (a) 31 GHz (for MA_{00} and MA_{10}) and (b) 38.5 GHz (for MA_{01} and MA_{11}) for the incident angle 0° and 40°, respectively.

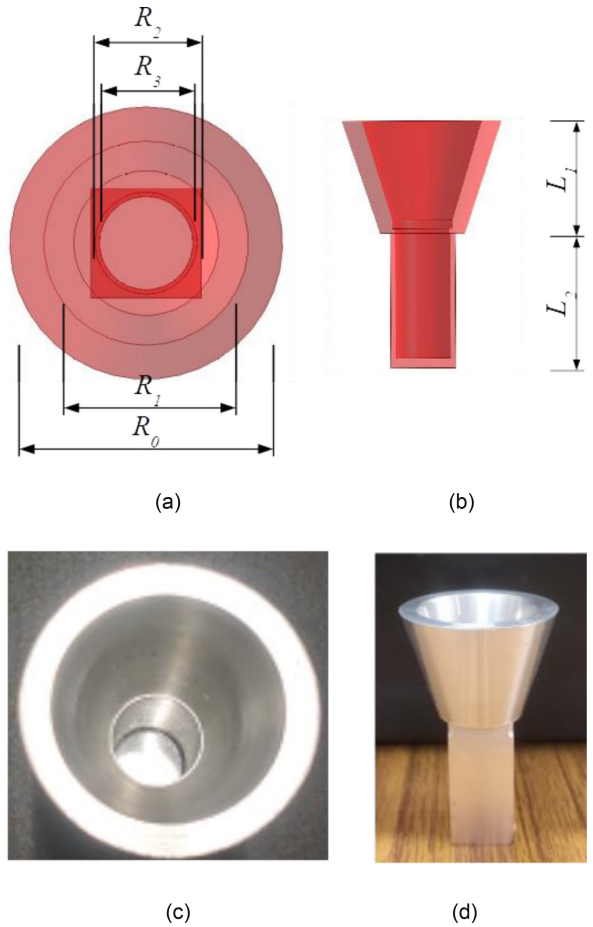

FIGURE 6. (a) Top and (b) side views of the Potter horn (PH). (c) Top and (d) side views of the fabricated PH.

The PH's schematic and fabricated prototype are shown in Fig. 4, with top and side views of the optimized structure in Fig. 6(a) and (b) and the fabricated prototype in Fig. 6(c) and (d). Key dimensions are R_0=32 mm, R_1=24 mm, R_2=12.8 mm, R_3=11 mm, L_1=24 mm, and L_2=26 mm.

The return loss (RL) of the fabricated Potter horn (PH) was measured using a Keysight FieldFox Microwave Analyzer N9951A [30], confirming operation from 20 GHz to 40 GHz, consistent with simulations (Fig. 7). The simulated PH feed shows slight discrepancies with the measured results, likely due to fabrication imperfections. However, the measured RL remains above 15 dB across the band, ensuring its suitability as the TA antenna's source feed. The realized gains, both simulated and measured, align closely across the band, as shown in Fig. 7, with gains exceeding 10 dBi throughout.

Radiation patterns at 30 GHz, depicted in Fig. 8(a), demonstrate well-matched, symmetrical *xoz*- and *yoz*-plane characteristics, with backlobe levels better than 20 dB and sidelobe levels (SLLs) below 15 dB. The proposed PH feed achieves a cross-polarization level of less than 30 dB. The 3-dB beamwidth varies between 22° and 11°, while the 10-dB edge taper ranges from 40° to 20° across the frequency band (Fig. 8(b)), corresponding to the slopes of 0.55°/GHz and 1°/GHz, respectively. These gradual slope

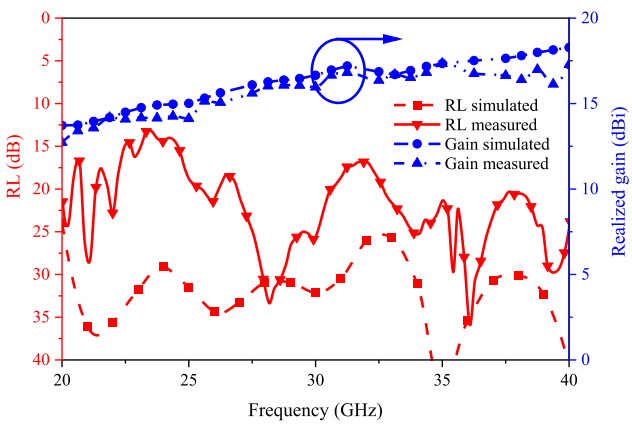

FIGURE 7. Return loss (RL) and realized gain (dBi) responses of the PH feed.

variations make the PH an ideal source feed for the TA antenna.

B. DESIGN OF WIDEBAND HIGH AE OF TA ANTENNA

The TA antenna aperture is constructed using four distinct 2-bit MAs (MA_{00}, MA_{01}, MA_{10}, and MA_{11}) to provide

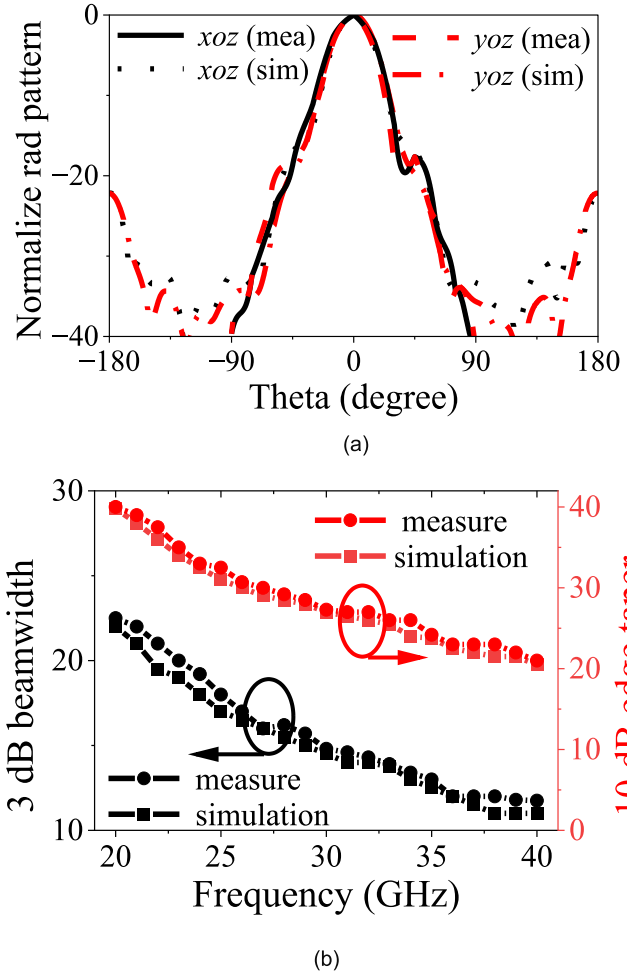

FIGURE 8. (a) Normalized radiation pattern [Mea-measured, and Sim-simulation] at 30 GHz and (b) frequency responses of 3-dB beamwidth and 10-dB edge taper of the PH.

the complete 360 transmission phase coverage. To ensure proper illumination and spherical-to-plane wave conversion, the PH feed is positioned at a unity focal ratio (F_T/D) to maintain PH taper below 30° to minimize spillover [21]. The aperture diameter is set at 90 mm, corresponding to an area of 63.58 λo^2. Each MA within the aperture dynamically compensates for the phase delay between the PH and the aperture, calculated using (3), where λo represents the free-space wavelength at 30 GHz, whereas x and y denote the longitudinal distributions.

$$\Phi(x,y) = \frac{2\pi}{\lambda_0}\left(\sqrt{x^2+y^2+F^2} - F\right) + \Phi_0 \tag{3}$$

Here, Φ_0 is a phase constant, implying a relative phase shift across transmitarray elements. Since the phase has been discretized into 4 distinct levels, (3) has been modified to (4) with proper incorporation of the discrete MAs, where m and n are the number of elements corresponding to the MA along x and y directions, while p is the periodicity.

$$\Phi(x,y) = \frac{2\pi}{\lambda_0}\left(\sqrt{(mp)^2+(np)^2+F^2} - F\right) + \Phi_0 \tag{4}$$

A circular aperture is chosen to enhance AE, surpassing rectangular and square designs [31]. It incorporates 729 elements, providing efficient illumination for the MS. The computed continuous phase distribution, depicted in Fig. 9(a), confirms uniform illumination across all the elements, thus achieving a seamless 360° phase coverage.

Fig. 9(b) represents the four-level quantized phase profile of the TA aperture. Each of the four MAs has a phase difference of 90°, and the phase compensation of each element has been set as follows: 0° ($0°<\Phi_i<90°$), 90° ($90°<\Phi_i<180$), 180° ($180<\Phi_i<270$), 270° ($270°<\Phi_i<360°$), respectively. In the design process, a continuous phase profile has been selected, followed by discretization for practical implementation. Notably, 729 elements are used to fill the maximum circular cross-sectional area for proper illumination of the TA aperture. The phase compensation of each element has been discretized as shown in Fig. 9(c). It is clearly observed from the illustration of Fig. 9(c) that, due to phase quantization, the design cannot produce the exact phase of the continuous phase profile; instead, some differences have been introduced towards the outer edge of the circular aperture. The TA circular aperture with the Potter horn has been simulated incorporating the Finite Element Boundary Integral (FEBI) boundary condition to reduce the usage of computational resources, consequently resulting in fast and accurate results for any complex structure instead of the conventional approach with radiation boundary conditions.

Fig. 10 presents the complex TA antenna and its simulated 3D radiation pattern. The 3D perspective view of the TA antenna is shown in Fig. 10(a), along with the simulated radiation pattern in Fig. 10(b) at 30 GHz.

The phase discontinuities can cause uneven current distribution on the antenna surface, leading to degraded radiation efficiency and increased SLLs. The proposed MA offers phase discontinuities of ±9° at 31 GHz and ±11.5° at 38.5 GHz. As shown in Fig. 11(a), the radiation pattern at these two frequencies demonstrates high directivity, with SLL suppression of at least 20 dB, while the *xoz*- and *yoz*-plane patterns offer symmetrical responses. Similarly, the current distribution has been spread evenly across the MA over the TA aperture, as referred to in Fig. 11(b); thus, the radiation patterns of the TA antenna in the two planes are independent of the phase discontinuities. The fabricated polarization rotator surface, consisting of 2-bit MAs, is shown along with its enlarged view in Fig. 12(a). The prototypes, consisting of top and bottom polarization-selective surfaces, are presented in Fig. 12(b) and (c), respectively, with their respective enlarged views. The three distinct layers are being aligned properly by

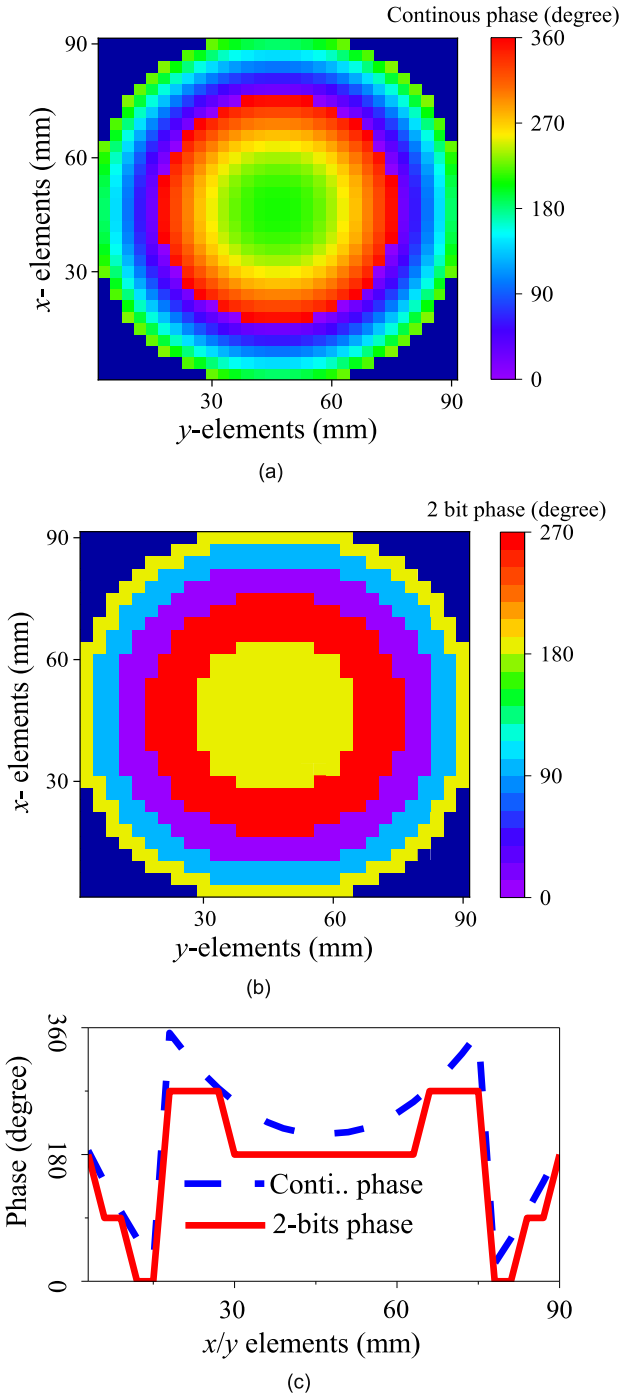

FIGURE 9. Computed phase distribution of the TA aperture (a) continuous phase profile, (b) 2-bit phase profile, (c) linear phase difference between continuous and 2-bit phase profile.

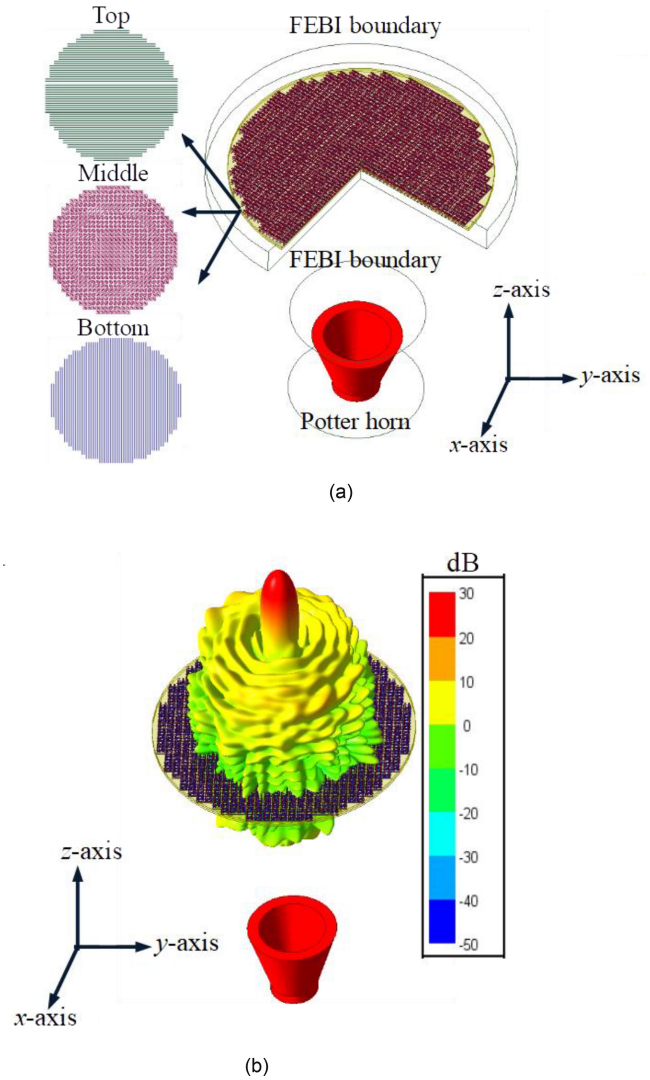

FIGURE 10. (a) The 3D perspective view of the TA antenna (TA aperture with Potter horn) simulated with the FEBI boundary, and (b) the 3D radiation patterns of the TA antenna at 30 GHz.

TABLE 2. Analysis of AE calculation.

Efficiency type	Sim (%)	Sim (dB)	Mea (%)	Mea (dB)
Spillover	93	0.27	93	0.32
Taper	87	0.60	86	0.65
Transmission	91	0.41	90	0.41
Other loss	85	0.71	81	0.92
Total (AE)	62.6	2.0	58.5	2.3

Sim stands for Simulation, and Mea stands for Measured

incorporating four dielectric screws placed at the corners of the RT5880 substrates.

V. EXPERIMENTAL VALIDATION OF WIDEBAND TA ANTENNA PERFORMANCE

The complete MS-based TA antenna is realized by placing the TA aperture and the PH assembly at the focal point of the aperture, as illustrated in Fig. 13(a). Notably, the phase center of the PH lies inside its mouth, which helps in placing the feed at the focal point to achieve maximum gain. The PH's position can be finely tuned, allowing it to be incrementally moved into the TA aperture for optimal performance. The TA antenna assembly is constructed using wood and Teflon with minimal metallic screws to prevent unwanted scattering during measurements, as depicted in Fig. 13(a). The return loss (RL) and radiation patterns are

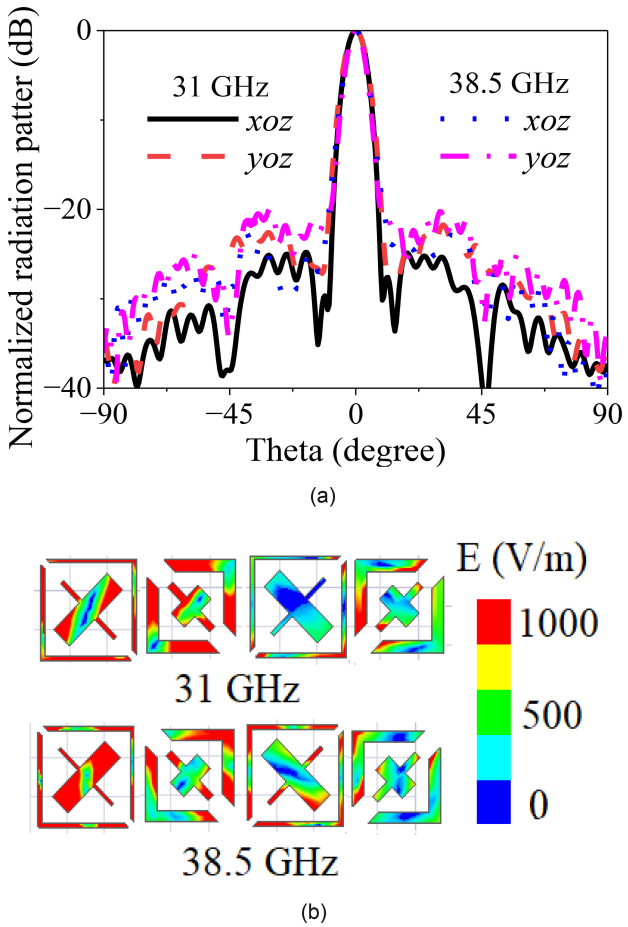

FIGURE 11. (a) Normalized radiation pattern (simulated) of TA antenna *xoz* and *yoz* plane at 31 GHz and 38.5 GHz, and (b) Electric field distribution of four distinct MA in the TA antenna at two spot frequencies (31 GHz and 38.5 GHz).

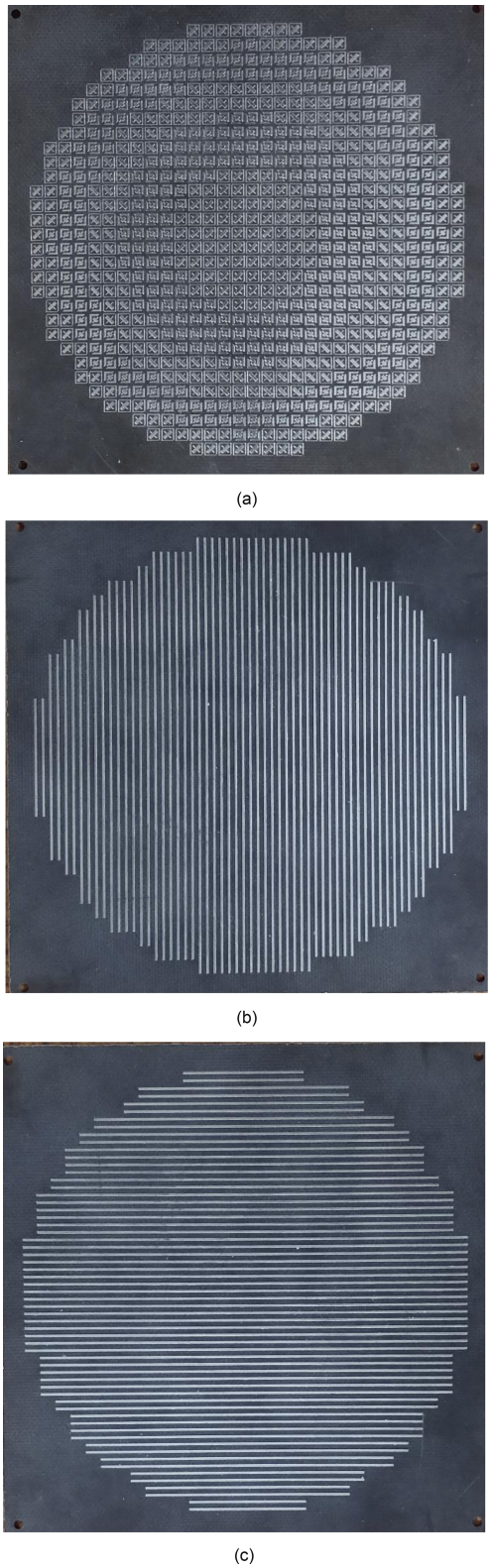

FIGURE 12. Fabricated prototype of (a) 2-bit MA polarization rotating surface, (b) top, and (c) bottom polarization selective surface.

rigorously evaluated in an anechoic chamber [32], with the measurement setup shown in Fig. 13(b).

To ensure accurate characterization, the RL and radiation patterns of the TA antenna prototype are measured using a Keysight FieldFox Microwave Analyzer (N9951A) [30]. The assembly's RL response, measured at the input of the PH, is compared with its simulated counterpart in Fig. 14, demonstrating reasonably good agreement between the simulation and experimental results. This meticulous approach ensures precise alignment, minimized interference, and reliable performance verification, enhancing the design's applicability in practical scenarios.

As observed from Fig. 14, the RL remains greater than 10 dB across the entire operational band (20 GHz to 40 GHz). A good agreement between the simulated and experimentally measured results is evident, with only a slight imbalance appearing in the low-frequency range, but the matching level is well below 10 dB. This discrepancy between the RL results on simulation and measurement arises possibly due to mode mismatch at lower frequencies, where the involvement of larger wavelengths leads to improper excitation or mode generation in the feed region, affecting the RL measurements of the TA antenna. The standard double-ridge horn antenna is used as the transmitter. In contrast, the

TABLE 3. Comparison between the proposed and reported wideband TA antennas.

Refer	f_0 (GHz)	Gain (dBi)	F/D	Polarization	Thickness (λ_0)	Type of unit cell	Phase range	AE (%)	1-dB /3-dB GBW (%)	SLLs (dB)
[4]	30	26.1	0.82	Single-LP	0.2	FSS	2-Bit	44.7	29.3/47	-18
[5]	10	27.2	1	Single-LP	0.05	FSS	2/4-Bit	40.7	16/24.7	-15
[6]	10	22.5	0.82	Single-LP	0.347	FSS	1-Bit	32	37/50	-16
[7]	100	28.7	1	Single-LP	0.202	FSS	2-Bit	38.2	NA/20	-20.5
[8]	23	25.7	1	Single-LP	0.210	ME-Dipole	2-Bit	53	–/38.7	-17
[9]	27	26.8	1.07	Single-LP	--	ME-Dipole	1-Bit	41	--/33	-18.5
[10]	25	29.3	1.15	Single-CP	0.24	Spiral-Dipole	3-bit	56.5	25.7/--	--
[11]	19.75	31.8	1	Single-CP	0.14	U-slot	3-Bit	60	15.2/--	-22
[12]	12	27.1	1	Dual-LP	0.12	L-patch	>360°	52.5	20.4/32.6	-18
[13]	9.7	28.4	1	Single-LP	--	PRE	3-bit	61.9	33.9/46.9	-20
This work	**32**	**27.3**	**1**	**Single-LP**	**0.157**	**M-FSS**	**2-Bit**	**58.5**	**39.68/49.2**	**-24**

F/D-focal length/diameter, LP-linear polarization, FSS-frequency selective surface, ME-magneto electric, AE-aperture efficiency, GBW-gain bandwidth, SLLs-side lobe levels, TA-transmitarray.

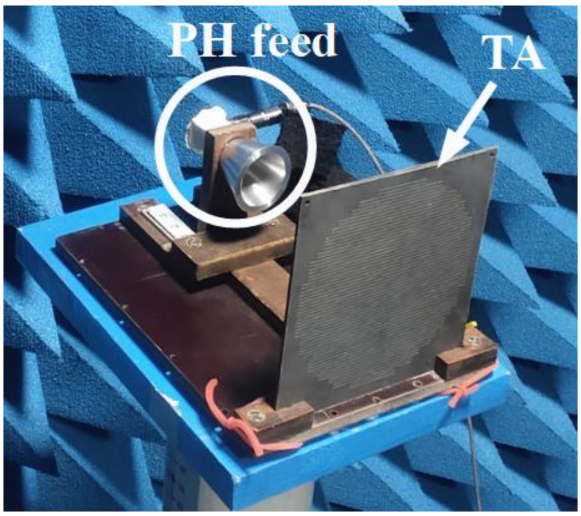

(a)

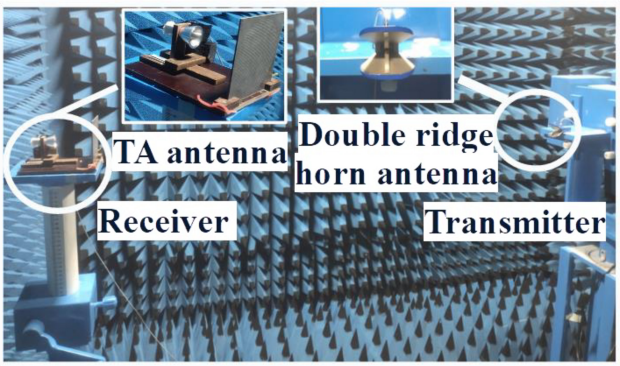

(b)

FIGURE 13. (a) Final assembly of the TA antenna (TA with PH). (b) Measurement setup of the TA antenna inside the anechoic chamber.

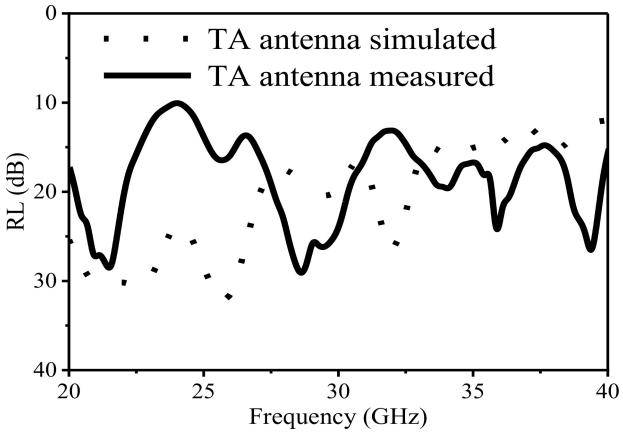

FIGURE 14. Frequency responses of RL (dB), of the proposed TA.

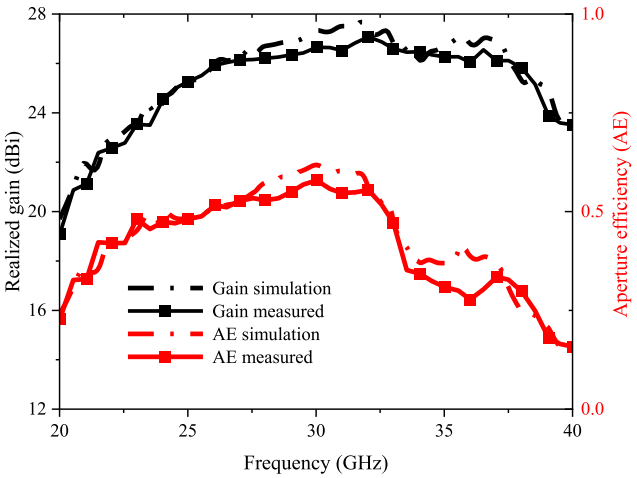

FIGURE 15. Realized gain (dBi) and AE along with the frequency of the proposed TA antenna.

fabricated TA antenna was placed on the receiving side to measure the TA antenna's gain, AE, and radiation pattern. The frequency response of the realized gain and the AE of the TA antenna is shown in Fig. 15, where it is compared with the simulated response and found to agree. The AE at a given frequency is computed using the conventional equation mentioned in (5).

$$\eta = \frac{\lambda^2 G_r}{4\pi A_p} \tag{5}$$

Here, λ is the wavelength, G_r is the realized gain (in linear units) of the TA antenna, and A_p is the physical aperture of the TA antenna.

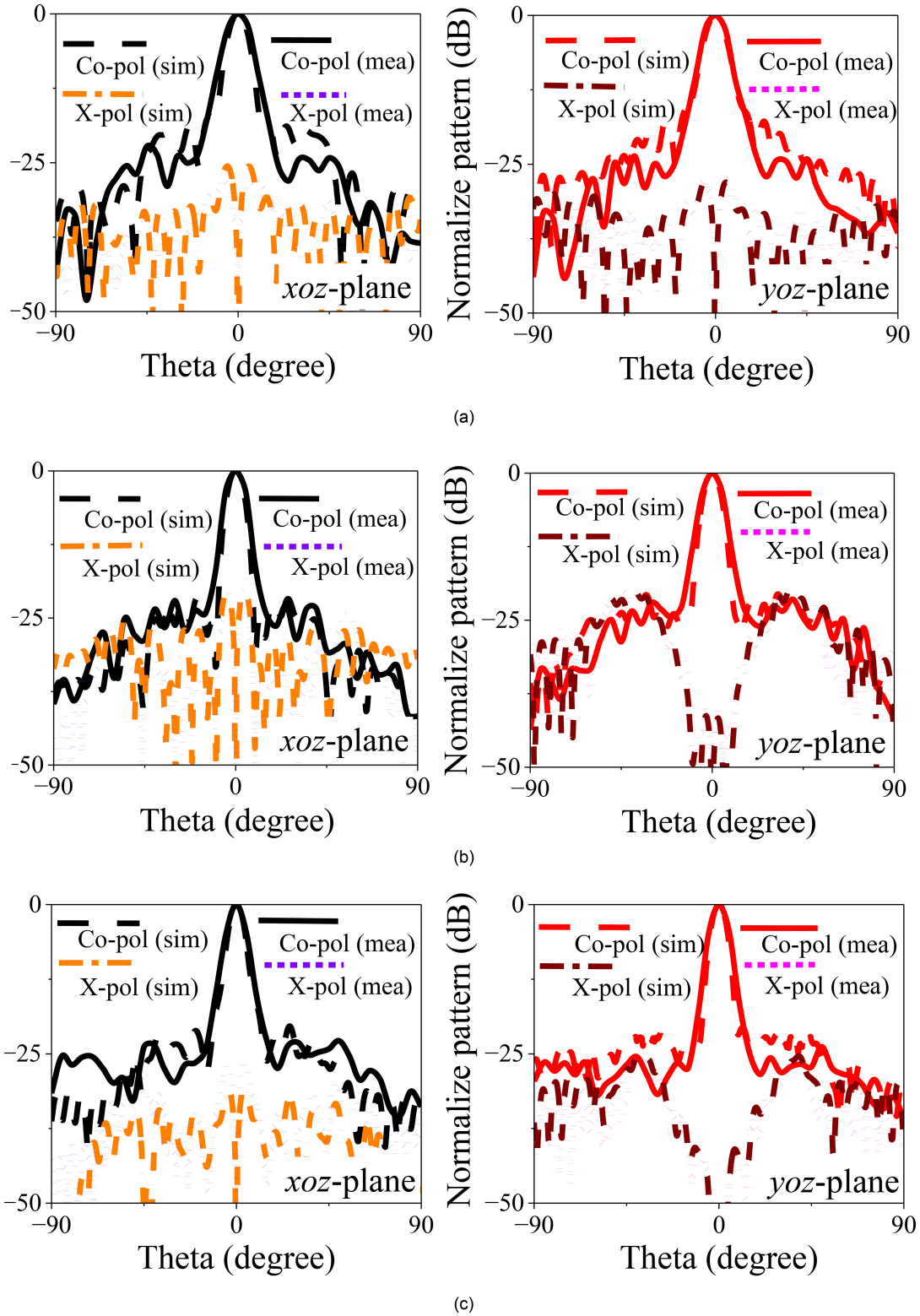

FIGURE 16. Normalized radiation pattern (dB) for the co-polarization (Co-pol) and cross-polarization (X-pol) of TA antenna for *xoz*- and *yoz*- plane at (a) 25 GHz, (b) 30 GHz, and (c) 35 GHz. [Note: - sim-simulation and mea-measured].

The realized gain is greater than 20 dBi throughout the band of interest, along with the peak realized gain of 27.2 dBi at 32 GHz, and the peak AE is found to be 58.5%, as illustrated in Fig. 15, while the relevant details have been listed in Table 2. A strong correlation is observed between the simulated and measured results for both realized

gain and AE, with slight deviations at select frequencies, primarily attributed to practical fabrication tolerances and measurement imperfections. This results in a 2.3 dB drop in the gain when compared to the theoretical directivity of the array. At 32 GHz, approximately 0.97 dB loss is attributed to the inefficiencies cause by the feed horn's taper and spillover [33]. An additional 0.41 dB reduction stems from transmission losses of the MAs and dielectric losses of the substrate. Moreover, the other factors, such as polarization mismatches, deviations in phase accuracy, and the oversimplified assumption of infinite periodicity, which neglects the role of edge elements, are likely responsible for a further 0.92 dB decrease in gain. The 1-dB and 3-dB GBWs have also been computed from Fig. 15 and found to be 12.69 GHz and 15.84 GHz, respectively, viz., 39.68% and 49.2% compared to the center frequency of 32 GHz.

Polarization and impedance mismatch between the feed and transmit array result in efficiency losses by reducing power transfer, followed by the introduction of phase errors. These issues, together with frequency-dependent losses, limit the system's usable bandwidth as well as the reduction of AE. The proposed TA antenna performs exceptionally well across various parameters, highlighting its innovative and advanced design. The normalized radiation patterns of the xoz- and yoz-plane are analyzed at three critical frequencies of 25 GHz, 30 GHz, and 35 GHz as shown in Fig. 16. An impressive achievement is the suppression of cross-polarized components, which remain over 20 dB below the main beam across all tested frequencies. Additionally, the sidelobe level (SLL) is maintained below 24 dB compared to the main beam, a significant improvement facilitated by the integration of subwavelength metasurfaces (MAs).

These MAs ensure a low SLL while preserving the antenna's broadband characteristics, a vital feature for modern communication systems. Furthermore, the optimized PH feed effectively minimizes edge diffraction, enhancing performance. The proposed TA antenna outperforms previously reported designs, as summarized in Table 3. It achieves a remarkable 15% improvement in AE and provides 20% wider 1-dB/3-dB GBWs compared/to its closest competitors [4], [5], [6][7], [9], [11], [12]. The combination of subwavelength MAs and an optimized PH feed assembly is resulting in a compact structure with a profile of just 0.157λ_o at 30 GHz. This configuration also achieves SLL suppression.

VI. CONCLUSION

In this paper, we present a low-profile, wideband metasurface-based TA antenna optimized for 20–40 GHz operation, setting a new benchmark for next-generation mm-wave applications. The design achieves a peak gain of 27.2 dBi, offering exceptional performance for demanding high-frequency systems. With broad 1-dB and 3-dB GBWs of 12.69 GHz and 15.84 GHz, respectively viz., 39.68% and 49.2%, and a maximum AE of 58.5%, the antenna delivers superior efficiency and wide operational bandwidth. The low SLLs, maintained below 24 dB across principal planes, ensure outstanding interference suppression and signal clarity. Experimental validation of the fabricated antenna confirms its high reliability, with measured results closely matching simulations. The proposed TA antenna tackles key challenges in mm-wave communications, delivering strong performance for satellite links and 5G/6G networks. Its innovative design enhances efficiency and versatility, contributing to advancements in modern wireless technologies. The current design focuses on achieving high directivity, low SLLs, and wide GBWs. Future work will explore integration and practical deployment for 5G/6G communication. The antenna's compact profile and wideband performance make it suitable for satellite and mm-Wave 5G/6G applications, where directional beams and efficient radiation are essential. Potential challenges include fabrication tolerances, environmental stability, and integration with transceiver systems, which will be addressed in forthcoming studies.

REFERENCES

[1] X. Ge, H. Cheng, G. Mao, Y. Yang, and S. Tu, "Vehicular communications for 5G cooperative small-cell networks," *IEEE Trans. Veh. Technol.*, vol. 65, no. 10, pp. 7882–7894, Oct. 2016.

[2] L. Di Palma, A. Clemente, L. Dussopt, R. Sauleau, P. Potier, and P. Pouliguen, "Radiation pattern synthesis for monopulse radar applications with a reconfigurable transmitarray antenna," *IEEE Trans. Antennas Propag.*, vol. 64, no. 9, pp. 4148–4154, Sep. 2016.

[3] Y. Ge, C. Lin, and Y. Liu, "Broadband folded transmitarray antenna based on an ultrathin transmission polarizer," *IEEE Trans. Antennas Propag.*, vol. 66, no. 11, pp. 5974–5981, Nov. 2018.

[4] P. Mei, G. F. Pedersen, and S. Zhang, "A broadband and FSS-based transmitarray antenna for 5G millimeter-wave applications," *IEEE Antennas Wireless Propag. Lett.*, vol. 20, pp. 103–107, 2021.

[5] K. Mavrakakis, H. Luyen, J. Booske, and N. Behdad, "Wideband transmitarrays based on polarization-rotating miniaturized-element frequency selective surfaces," *IEEE Trans. Antennas Propag.*, vol. 68, no. 3, pp. 2128–2137, Mar. 2020.

[6] S. Liu, H. Sato, and Q. Chen, "A wideband, 1 bit transmitarray antenna design with flat gain response," *IEEE Trans. Antennas Propag.*, vol. 68, no. 10, pp. 7046–7055, Oct. 2020.

[7] S. Shi, Q. Lu, W. Feng, and W. Chen, "Wideband polarization rotation transmitarray using arrow-shaped FSS at W-band," *IEEE Trans. Antennas Propag.*, vol. 70, no. 7, pp. 6001–6005, Jul. 2022.

[8] B. J. Xiang, X. Dai, and K.-M. Luk, "A wideband 2-bit transmitarray antenna for millimeter-wave vehicular communication," *IEEE Trans. Veh. Technol.*, vol. 71, no. 9, pp. 9202–9211, Sep. 2022.

[9] F. Wu, L. Xiang, J. Wang, K.-M. Luk, and W. Hong, "A hybrid-element approach to design wideband ME-dipole transmitarray with improved aperture efficiency," *IEEE Antennas Wireless Propag. Lett.*, vol. 21, pp. 1338–1342, 2022.

[10] B. Zheng, Y. Fan, and Y. J. Cheng, "A wideband circularly polarized transmitarray using matched dipole-spiral elements," *IEEE Antennas Wireless Propag. Lett.*, vol. 23, pp. 1196–1200, 2024.

[11] B. Zheng, Y. Fan, and Y. J. Cheng, "Wideband high-efficiency circularly polarized transmitarray with linearly polarized feed," *IEEE Antennas Wireless Propag. Lett.*, vol. 22, pp. 1451–1455, 2023.
[12] T. Yin et al., "Wideband high-efficiency transmitarray antenna using compact double-layer dual-linearly polarized elements," *IEEE Antennas Wireless Propag. Lett.*, vol. 22, pp. 2372–2376, 2023.
[13] J. Zhao et al., "A high aperture efficiency and wideband transmitarray antenna using novel double c-shaped elements," *IEEE Antennas Wireless Propag. Lett.*, vol. 23, pp. 4024–4028, 2024.
[14] S. Bhattacharyya, "Metamaterials and metasurfaces for high frequency applications," in *Photonics, Plasmonics and Information Optics: Research and Technological Advances*. Boca Raton, FL, USA: CRC Press, 2021, ch. 3, pp. 31–65.
[15] S. K. Ghosh, S. Das, and S. Bhattacharyya, "Graphene-based metasurface for tunable absorption and transmission characteristics in the near mid-infrared region," *IEEE Trans. Antennas Propag.*, vol. 70, no. 6, pp. 4600–4612, Jun. 2022.
[16] S. Chatterjee, Y. Gupta, S. K. Ghosh, and S. Bhattacharyya, "RFI mitigation of radio astronomical receiver using a low-profile metasurface-loaded antenna," *IEEE Trans. Electromagn. Compat.*, vol. 66, no. 1, pp. 108–117, Feb. 2024.
[17] D. Samantaray, S. K. Ghosh, and S. Bhattacharyya, "Modified slotted patch antenna with metasurface as superstrate for dual-band applications," *IEEE Antennas Wireless Propag. Lett.*, vol. 22, pp. 109–113, 2023.
[18] M. Chandra, Nilotpal, D. Samantaray, M Thottappan, and S. Bhattacharyya, "A broadband transmissive type metasurface cross-polarization converter for EMC application," *IEEE Trans. Electromagn. Compat.*, vol. 65, no. 1, pp. 186–194, Feb. 2023.
[19] S. Liu and Q. Chen, "A wideband, multifunctional reflect-transmit-array antenna with polarization-dependent operation," *IEEE Trans. Antennas Propag.*, vol. 69, no. 3, pp. 1383–1392, Mar. 2021.
[20] R. L. Haupt, "Antenna design with a mixed integer genetic algorithm," *IEEE Trans. Antennas Propag.*, vol. 55, no. 3, pp. 577–582, Mar. 2007.
[21] P. Nayeri, F. Yang, and A. Z. Elsherbeni, *Reflectarray Antennas: Theory, Designs, and Applications*, Hoboken, NJ, USA: Wiley, 2018.
[22] H. Li, G. Wang, T. Cai, H. Hou, and W. Guo, "Wideband transparent beam-forming metadevice with amplitude- and phase-controlled metasurface," *Phys. Rev. Appl.*, vol. 11, no. 1, Jan. 2019, Art. no. 14043.
[23] T.-J. Li, G.-M. Wang, T. Cai, H.-P. Li, J.-G. Liang, and J. Lou, "Broadband folded transmitarray antenna with ultralow-profile based on metasurfaces," *IEEE Trans. Antennas Propag.*, vol. 69, no. 10, pp. 7017–7022, Oct. 2021.
[24] (ANSYS Inc., Canonsburg, PA, USA). *Ansys HFSS*. Accessed: Aug. 11, 2025. [Online]. Available: https://www.ansys.com/en/in/products/electronics/ansys-hfss
[25] C. Mentzer and L. Peters, "Pattern analysis of corrugated horn antennas," *IEEE Trans. Antennas Propag.*, vol. 24, no. 3, pp. 304–309, May 1976.
[26] S. K. Rao, C.-C. Hsu, and K. K. Chan, "Antenna system supporting multiple frequency bands and multiple beams," *IEEE Trans. Antennas Propag.*, vol. 56, no. 10, pp. 3327–3329, Oct. 2008.
[27] K. K. Chan and S. K. Rao, "Design of high-efficiency circular horn feeds for multibeam reflector applications," *IEEE Trans. Antennas Propag.*, vol. 56, no. 1, pp. 253–258, Jan. 2008.
[28] P. D. Potter, "A new horn antenna with suppressed sidelobes and equal beamwidths," *Microw. J.*, vol. 18, no. 2, pp. 71–78, Jun. 1961.
[29] L. Shafai, S. K. Sharma, and S. Rao, *Handbook of Reflector Antennas and Feed Systems, Volume II: Feed Systems*. Norwood, MA, USA: Artech House, 2013.
[30] (Keysight Technol., Santa Rosa, CA, USA). *N9951A FieldFox Handheld Microwave Analyzer, 44 GHz*. Accessed: Aug. 11, 2025. [Online]. Available: https://www.keysight.com/us/en/product/N9951A/fieldfox-a-handheld-microwave-analyzer-44-ghz.html
[31] W. L. Stutzmann and G. A. Thiele, *Antenna Theory & Design*. Hoboken, NJ, USA: Wiley, 1981)
[32] (Appl. Concept Group, Middletown, CE, USA). *RF Anechoic Chamber*. Accessed: Aug. 11, 2025. [Online]. Available: http://www.applied-cg.in/rf-anechoic-chamber-2/
[33] R. E. Collin, *Antennas and Radiowave Propagation*. New York, NY, USA: McGraw-Hill, 1985.

SOUGATA CHATTERJEE (Graduate Student Member, IEEE) received the Bachelor of Technology degree in electronics and communication engineering from the West Bengal University of Technology, India, in 2007, and the Master of Technology degree in microwave engineering from the University of Burdwan, Burdwan, India, in 2010. From June 2010 to May 2012, he was a Research Scientist with SAMEER Kolkata. Since May 2012, he has been a Scientific Officer in GMRT-NCRA-TIFR. He is currently pursuing the external Ph.D. degree with the Department of Electronics and Communication Engineering, IIT-BHU, Varanasi, India. His research interests include metasurface antennas and computational electromagnetics. He is a recipient of the prestigious 2025 IEEE Antennas and Propagation Society Doctoral Research Grant.

YASHWANT GUPTA (Senior Member, IEEE) received the bachelor's degree in electrical engineering from IIT Kanpur in 1985, and the M.S. and Ph.D. degrees in radio astronomy from the University of California at San Diego, San Diego, CA, USA, in 1990,

He is currently a Distinguished Professor with the Tata Institute of Fundamental Research, heads TIFR's National Centre for Radio Astrophysics, Pune, as the Centre Director. In particular, he has contributed significantly to the building and running of the Giant Metrewave Radio Telescope Observatory—a World-Class Facility located near Pune and operated by NCRA—right from its conceptualization to its recent upgrade. He also spearheads India's participation in the Square Kilometre Array Project—an international collaborative project to design and build the next generation global radio astronomy facility. He has published more than 170 research articles in international journals, and has also delivered plenary speeches and keynote addresses in several international and national-level meetings. He is known for his research on pulsars (which are very rapidly rotating, highly magnetized neutron stars) and the interstellar medium, as well as the development of instrumentation and signal processing techniques for radio astronomy.

Prof. Gupta has also been honoured with a number of awards, such as in 2007, he was conferred the Shanti Swarup Bhatnagar Prize for Science and Technology by the Council of Scientific and Industrial Research, Government of India—one of the highest science awards in India, for his contributions to physical sciences, for his contributions. In 2022, he was conferred the Murli M. Chugani Memorial Award of the Indian Physics Association, for his achievements in applied physics. In 2023, he was conferred the Distinguished Alumnus Award of IIT Kanpur. He has been elected to all the major national academies of science and engineering in India, such as INAE, INSA, NASI, and IASc. More recently, in 2019, he and his team have been awarded the Zubin Kembhavi Award by the Astronomical Society of India, for the work of the upgrade of GMRT. He is a member of several professional bodies, such as The International Astronomical Union and the International Union of Radio Science.

SATISH KUMAR SHARMA (Fellow, IEEE) received the B.Tech. degree in electronics engineering from the Kamla Nehru Institute of Technology in 1991, and the Ph.D. degree in electronics engineering from the Indian Institute of Technology, Banaras Hindu University in 1997. From March 1999 to April 2001, he was a Postdoctoral Fellow with the Department of Electrical and Computer Engineering, University of Manitoba, Winnipeg, Canada. He was a Senior Antenna Engineer with InfoMagnetics Technologies Corporation, Winnipeg, from May 2001 to August 2006. Simultaneously, he was also a Research Associate with the University of Manitoba from June 2001 to August 2006. In August 2006, he joined the Department of Electrical and Computer Engineering, San Diego State University, San Diego, USA, as an Assistant Professor. Here, he has developed an the Antenna Laboratory, teaches courses in applied electromagnetics, and advises B.S., M.S., and Ph.D. students and Postdoctoral Fellows. Since 2014, he has been a Full Professor and the Director of the Antenna and Microwave Laboratory. He has authored/co-authored more than 340 research papers published in the referenced international journals and conferences. He has co-edited three volumes of Handbook of Reflector Antennas and Feed Systems, *Volume 1: Theory and Design of Reflectors*, *Volume II: Feed Systems*, and *Volume III: Applications of Reflectors* (Artech House, USA). His new coedited/co-authored book, *Multifunctional Antennas and Arrays for Wireless Communication Systems* (IEEE Press/Wiley, USA). His main research interests are in the millimeter wave antennas, flat panel phased array antennas/beam steering antennas, massive MIMO antennas, 5G communication antennas, antennas for IoT, miniaturized antennas, ultra-wideband, multiband and broadband antennas, reconfigurable and frequency agile antennas, feeds for reflector antennas, waveguide horns and polarizers, electrically small antennas, RFID antennas, active antennas, frequency selective surfaces, metasurfaces, and microwave passive components. He received the IEEE AP-S Harold A. Wheeler Prize Paper Award in 2015, the National Science Foundation's Faculty Early Development (CAREER) Award in 2009, and the Young Scientist Award of URSI Commission B, Field and Waves, during the URSI Triennial International Symposium on Electromagnetic Theory, Pisa, Italy, in 2004. He was recognized as the Outstanding Associate Editor (AE) for the IEEE Transactions on Antennas and Propagation in July 2014. He served as the AE for the IEEE TRANSACTIONS ON ANTENNAS AND PROPAGATION and the IEEE ANTENNAS AND WIRELESS PROPAGATION LETTERS. He is currently serving the IEEE AP-Society as its Distinguished Lecturer, an Administrative Committee Member, a Fellow Evaluation Committee, and the Chair of the TC9: Security.

SOMAK BHATTACHARYYA (Senior Member, IEEE) received the Bachelor of Technology and Master of Technology degree from the Institute of Radio Physics and Electronics, University of Calcutta, India, in 2006 and 2008, respectively, and the Ph.D. degree from the Indian Institute of Technology, Kanpur, India, in 2015.

Since 2016 December, he has been associated with the Department of Electronics Engineering, Indian Institute of Technology (Banaras Hindu University), Varanasi, India, where he is currently serving as an Associate Professor. His current areas of interest lie in metamaterial, metasurface, periodic structures, and opto-microwave devices. He has received the prestigious Young Scientist Award from International Union of Radio Sciences three times. He has been elected as a Life Fellow of OSI, a Fellow of IETE, and an Associate Fellow of West Bengal Academy of Science and Technology. He is one of the two representatives from his country to serve in the Speakers Bureau Program in IEEE MTT-S. He has been conferred with the Outstanding Volunteer Award of 2024 IEEE MTT-S R-10, the IEEE UP Section Outstanding Section Volunteer Award 2022, the IETE Smt. Manorama Rathore Memorial Award 2022, the Innovation Award in Microwave Field-2021 from IEEE AP/MTT Joint Chapter Gujarat Section. He also has mentored IEEE MTT-S Student Branch Chapter IITBHU Varanasi to be adjudged as the Outstanding Chapter Award from both IEEE MTT-S and IEEE UP Section in 2022.